

# Fluorescence imaging of nanoscale domains in polymer blends using stochastic optical reconstruction microscopy (STORM)

M. W. Gramlich,<sup>1</sup> J. Bae,<sup>2</sup> R. C. Hayward,<sup>2</sup> and J. L. Ross<sup>1,\*</sup>

<sup>1</sup>Department of Physics, University of Massachusetts-Amherst, Amherst, Massachusetts 01039, USA

<sup>2</sup>Department of Polymer Science and Engineering, University of Massachusetts-Amherst, Amherst, Massachusetts 01039, USA

\*rossj@physics.umass.edu

**Abstract:** High-resolution fluorescence techniques that provide spatial resolution below the diffraction limit are attractive new methods for structural characterization of nanostructured materials. For the first time, we apply the super-resolution technique of Stochastic Optical Reconstruction Microscopy (STORM), to characterize nanoscale structures within polymer blend films. The STORM technique involves temporally separating the fluorescence signals from individual labeled polymers, allowing their positions to be localized with high accuracy, yielding a high-resolution composite image of the material. Here, we describe the application of the technique to demixed blend films of polystyrene (PS) and poly(methyl methacrylate) (PMMA), and find that STORM provides comparable structural characteristics as those determined by Atomic Force Microscopy (AFM) and scanning electron microscopy (SEM), but with all of the advantages of a far-field optical technique

©2014 Optical Society of America

**OCIS codes:** (160.1245) Artificially engineered materials; (180.2520) Fluorescence microscopy; (110.3010) Image reconstruction techniques

---

## References and links

1. M. Born and E. Wolf, *Principles of optics: electromagnetic theory of propagation, interference and diffraction of light*, (Cambridge University Press, Cambridge, 1999).
2. A. Neumann, Y. Kuznetsova, and S. R. J. Brueck, "Structured illumination for the extension of imaging interferometric microscopy," *Opt. Express* **16**(10), 6785–6793 (2008).
3. T. R. Hillman, T. Gutzler, S. A. Alexandrov, and D. D. Sampson, "High-resolution, wide-field object reconstruction with synthetic aperture Fourier holographic optical microscopy," *Opt. Express* **17**(10), 7873–7892 (2009).
4. T. Zhang, Y. Ruan, G. Maire, D. Sentenac, A. Talneau, K. Belkebir, P. C. Chaumet, and A. Sentenac, "Full-polarized Tomographic Diffraction Microscopy Achieves a Resolution about One-Fourth of the Wavelength," *Phys. Rev. Lett.* **111**(24), 243904 (2013).
5. K. Lee, H. D. Kim, K. Kim, Y. Kim, T. R. Hillman, B. Min, and Y. Park, "Synthetic Fourier transform light scattering," *Opt. Express* **21**(19), 22453–22463 (2013).
6. S. Arhab, G. Soriano, Y. Ruan, G. Maire, A. Talneau, D. Sentenac, P. C. Chaumet, K. Belkebir, and H. Giovannini, "Nanometric Resolution with Far-Field Optical Profilometry," *Phys. Rev. Lett.* **111**(5), 053902 (2013).
7. C. G. Galbraith and J. A. Galbraith, "Super-resolution microscopy at a glance," *J. Cell Sci.* **124**(10), 1607–1611 (2011).
8. M. Bates, T. R. Blosser, and X. Zhuang, "Short-Range Spectroscopy Ruler Based on a Single-Molecule Optical Switch," *Phys. Rev. Lett.* **94**(10), 108101 (2005).
9. M. J. Rust, M. Bates, and X. W. Zhuang, "Sub-diffraction-limit imaging by stochastic optical reconstruction microscopy (STORM)," *Nat. Methods* **3**(10), 793–796 (2006).
10. J. Fölling, M. Bossi, H. Bock, R. Medda, C. A. Wurm, B. Hein, S. Jakobs, C. Eggeling, and S. W. Hell, "Fluorescence nanoscopy by ground-state depletion and single-molecule return," *Nat. Methods* **5**(11), 943–945 (2008).
11. G. T. Dempsey, J. C. Vaughan, K. H. Chen, M. Bates, and X. Zhuang, "Evaluation of fluorophores for optimal performance in localization-based super-resolution imaging," *Nat. Methods* **8**(12), 1027–1036 (2011).

12. E. Betzig, G. H. Patterson, R. Sougrat, O. W. Lindwasser, S. Olenych, J. S. Bonifacino, M. W. Davidson, J. Lippincott-Schwartz, and H. F. Hess, "Imaging Intracellular Fluorescent Proteins at Nanometer Resolution," *Science* **313**(5793), 1642–1645 (2006).
13. S. T. Hess, T. P. K. Girirajan, and M. D. Mason, "Ultra-High Resolution Imaging by Fluorescence Photoactivation Localization Microscopy," *Biophys. J.* **91**(11), 4258–4272 (2006).
14. S. W. Hell and J. Wichmann, "Breaking the diffraction resolution limit by stimulated emission: stimulated-emission-depletion fluorescence microscopy," *Opt. Lett.* **19**(11), 780–782 (1994).
15. S. W. Hell, "Far-field optical nanoscopy," *Science* **316**(5828), 1153–1158 (2007).
16. G. Moneron, R. Medda, B. Hein, A. Giske, V. Westphal, and S. W. Hell, "Fast STED microscopy with continuous wave fiber lasers," *Opt. Express* **18**(2), 1302–1309 (2010).
17. S. W. Hell, "Fluorescent Dyes Used in STED microscopy," <http://nanobiophotonics.mpibpc.mpg.de/old/dyes/> (2014).
18. C. K. Ullal, R. Schmidt, S. W. Hell, and A. Egner, "Block Copolymer Nanostructures Mapped by Far-Field Optics," *Nano Lett.* **9**(6), 2497–2500 (2009).
19. J. L. Ross and R. Dixit, *Methods in Cell Biology*, (Elsevier, 2010), Chap. 26.
20. S. A. Jones, S.-H. Shim, J. He, and X. Zhuang, "Fast, three-dimensional super-resolution imaging of live cells," *Nat. Methods* **8**(6), 499–505 (2011).
21. S. W. Hell, "Microscopy and its focal switch," *Nat. Methods* **6**(1), 24–32 (2009).
22. B. Huang, W. Wang, M. Bates, and X. Zhuang, "Three-Dimensional Super-Resolution Imaging by Stochastic Optical Reconstruction Microscopy," *Science* **319**(5864), 810–813 (2008).
23. R. Henriques, M. Lelek, E. F. Fornasiero, F. Valtorta, C. Zimmer, and M. M. Mhlanga, "QuickPALM: 3D real-time photoactivation nanoscopy image processing in ImageJ," *Nat. Methods* **7**(5), 339–340 (2010).
24. C. A. Schneider, W. S. Rasband, and K. W. Eliceiri, "NIH Image to ImageJ: 25 years of image analysis," *Nat. Methods* **9**(7), 671–675 (2012).
25. F. Huang, S. L. Schwartz, J. M. Byars, and K. A. Lidke, "Simultaneous multiple-emitter fitting for single molecule super-resolution imaging," *Biomed. Opt. Express* **2**(5), 1377–1393 (2011).
26. H. T. Ho, M. E. Levere, S. Pascual, V. Montebault, J. C. Soutif, and L. Fontaine, "Phosphites as alternative coreagents for the one-pot aminolysis/thiol-ene synthesis of maleimide-functionalized RAFT polymers," *J. Polym. Sci. A Polym. Chem.* **50**(8), 1657–1661 (2012).
27. S. H. Lee, M. Baday, M. Tjioe, P. D. Simonson, R. Zhang, E. Cai, and P. R. Selvin, "Using fixed fiducial markers for stage drift correction," *Opt. Express* **20**(11), 12177–12183 (2012).
28. L. Sung, A. Karim, J. F. Douglas, and C. C. Han, "Dimensional crossover in the phase separation kinetics of thin polymer blend films," *Phys. Rev. Lett.* **76**(23), 4368–4371 (1996).
29. F. Wagner and J. M. Yeomans, "Breakdown of Scale Invariance in the Coarsening of Phase-Separating Binary Fluids," *Phys. Rev. Lett.* **80**(7), 1429–1432 (1998).
30. S. Walheim, M. Böltau, J. Mlynek, G. Krausch, and U. Steiner, "Structure Formation via Polymer Demixing in Spin-Cast Films," *Macromolecules* **30**(17), 4995–5003 (1997).
31. L. Li, X. Shen, S. W. Hong, R. C. Hayward, and T. P. Russell, "Fabrication of Co-continuous Nanostructured and Porous Polymer Membranes: Spinodal Decomposition of Homopolymer and Random Copolymer Blends," *Angew. Chem. Int. Ed. Engl.* **51**(17), 4089–4094 (2012).

## 1. Introduction

Imaging of materials on the nanometer scale has traditionally relied primarily on the use of electron and scanning probe microscopy. While atomic force microscopy (AFM) and scanning electron microscopy (SEM) can provide nanometer-scale resolution with minimal sample treatment (Fig. 1) these techniques are suitable for measuring only the surface of a material, and thus require destructive sample etching or cross sectioning to visualize internal structures. Similarly, transmission electron microscopy (TEM) can provide atomic-level structural information, but requires samples to be fixed and cut into very thin sections. In contrast, conventional optical microscopy (OM) techniques allow for non-invasive, three-dimensional imaging of dynamic samples without the need for fixing or sectioning, but suffer from a spatial resolution limit of about 200–250 nm due to the diffraction limit of light [1]. Recently, optical interference techniques, such as optical coherence tomography (OCT) [2–5] or optical diffractive tomographic microscopy (ODTM) [6], can break the diffraction limit and provide high resolution three dimensional imaging. These techniques have been used for biological [5] as well as synthetic samples [2–4, 6]. However, such diffraction techniques require extensive Fourier transform algorithms and angle optimization resulting in permittivity maps of the surface. Therefore, this technique can miss dynamics between two interacting materials of the same permittivity.

Recently, advances in fluorescence techniques have pushed the resolution level well below the diffraction limit, approaching electron microscopy-level resolution while maintaining the advantages of OM for three dimensional imaging of dynamic and solvated systems [7]. Although these techniques have been developed primarily for biological imaging, they offer exciting promise for studying structure and dynamics in synthetic materials as well. There are several methods to accomplish super-resolution of fluorescent samples including: STochastic Optical Reconstruction Microscopy (STORM) with activator-reporter dye pairs [8, 9], or STORM with single dyes, called direct-STORM (dSTORM) [10, 11], Photo-Activated Localization Microscopy (PALM) [12, 13], or STimulated Emission and Depletion (STED) microscopy [14, 15]. STED originally relied on special fluorophores and complicated, high-power laser systems that were not widely available. The current state-of-the art in STED imaging uses less expensive CW lasers [16] and a wider range of commercially available dyes [17], making the instruments less costly, easier to maintain, and more common. STED has been successfully used to resolve microphase-separated domains in block-copolymer thin films [18]. However, STED is a line-scanning technique, which ultimately limits the time-resolution required for dynamic samples. Further, the optics required for STED is still advanced and expensive limiting the ability of novice builders or those at smaller institutions to have access to this technique.

Alternatively, the STORM instrument is just a simple total internal reflection fluorescence (TIRF) microscopy design that uses a single laser for activation and imaging of common fluorophores [11, 19], making it a simpler technique. PALM is the same optical and analysis technique as STORM except it uses genetically encoded fluorophores, making it well-suited to the study of cellular systems, but inconvenient for most other applications; consequently we did not utilize PALM here. So far, STORM has been successfully employed in biological systems with lateral resolution down to 20 nm [7–9, 11] and three-dimensional (3D) imaging using optical astigmatism to provide axial resolution of 50–60 nm [20–22], but its application to synthetic material systems remains largely unexplored.

STORM works by temporally separating the emission from individual fluorophores that would normally overlap within a densely labeled structure. The temporal separation occurs by inducing the majority of fluorophores into a long-lived quantum state that is non-fluorescent. Individual fluorophores can emerge from this state stochastically allowing only a few fluorophores to be active at a time, and they are observed to “blink” [9]. If the individual, fluorescent-state fluorophores are spatially separated, they can each be localized with high accuracy using centroid or Gaussian fitting to the intensity profile, or point-spread function. The locations of individual point spread functions are then recombined into a single reconstructed image. Data acquisition involves many exposures (>500) of the randomly blinking fluorophores, to obtain the final reconstruction. Freely available software packages, such as quickPALM [23] for ImageJ [24], or MATLAB [25], are used to localize individual fluorophores within each frame with high spatial resolution, and then combine fitted positions into a single high-resolution image.

In this paper, we use a simple model material system consisting of de-mixed blended films of polystyrene (PS) and poly(methyl methacrylate) (PMMA) to demonstrate the utility of STORM for characterization of synthetic nanostructured materials. The de-mixed structures, formed as solvent is evaporated during spin coating, consist of PMMA-rich droplet domains within a PS-rich matrix. The sizes of PMMA domains are varied from ~100 – 400 nm depending on the film thickness. Thus, the PS/PMMA provides an excellent model to test the capabilities of STORM above and below the diffraction limit of standard fluorescence techniques.

Here, we describe the methodology necessary for imaging the PS/PMMA polymer samples. We employ a glycerol based imaging solution to avoid issues of fluorophore bleaching encountered for aqueous buffers. We highlight the necessity of fluorophore drift correction in order to obtain the high resolution of the technique. Finally, we discuss the

analysis used to quantitatively fit individual PMMA domains. Using this methodology, we present the evolution of PMMA-rich domain size and density as a function of film thickness.

## 2. Experimental materials and setup

### 2.1 Synthesis and Aminolysis of poly(methyl methacrylate) and end-functionalization with Alexa Fluor 647®:

Methyl methacrylate (2 g, 20 mmol) was added to a 25 mL, two-necked round bottom flask equipped with a septum and a condenser topped with a gas inlet. 2-cyano-2-propyl dodecyl trithiocarbonate (CPDT) (0.028 g, 0.08 mmol) was dissolved in 0.7 mL toluene and added to the reaction flask. A stock solution of 1 mg/mL AIBN in toluene was prepared, and 1.3 mL (1.3 mg, 0.008 mmol) of this solution was added to the reaction flask. The mixture was degassed using three freeze-pump-thaw cycles, and then immersed in an oil bath set to 80 °C and stirred for 18 h under nitrogen. The polymer was precipitated into methanol, isolated by filtration, and dried under vacuum to afford a light yellow powder (0.85 g, 58%). The conversion was calculated as 72% by <sup>1</sup>H NMR in CDCl<sub>3</sub>. SEC (THF vs. PMMA standards): M<sub>n</sub> = 15300 g/mol, PDI = 1.22. <sup>1</sup>H NMR (300 MHz, CDCl<sub>3</sub>): δ = 3.59 (s, 3H), 3.23 (s, 2H CPDT), 2.09-0.70 (m, 5H). <sup>13</sup>C NMR (75 MHz, CDCl<sub>3</sub>): δ = 177.74, 176.88, 54.37, 51.75, 44.48, 18.65, 16.41.

Similar to the procedure previously reported [26], poly(methyl methacrylate) (11 mg, 0.7 μmol) was dissolved in 0.2 mL DMF. Triethyl phosphite (1 μL, 6 μmol) and hexyl amine (1 μL, 8 μmol) were added to the mixture, which was degassed using three freeze-pump-thaw cycles then stirred 3 h at room temperature under nitrogen. Alexa Fluor 647 maleimide (1 mg, 0.7 μmol) was dissolved in 0.1 mL DMF. TEA (1 μL, 3 μmol) was added to this solution, which was then transferred to the poly(methyl methacrylate) solution. The reaction mixture was stirred 18 h at room temperature under nitrogen, then dialyzed against chloroform in a 6-8 kDa molecular weight cut-off membrane. Chloroform was removed under reduced pressure. To remove any remaining free dye, the polymer was dissolved in 6 mL THF and centrifuged four times for 15 minutes at 4000 RPM. THF was removed under reduced pressure, the polymer obtained as a blue solid (12 mg, >99%), and analyzed by HPLC. Size exclusion HPLC (λ<sub>ex</sub> = 650 nm, λ<sub>em</sub> = 665 nm) revealed 42% fluorescently labeled polymer by peak area.

### 2.2 Sample preparation

The blend solutions of PS and PMMA (50:50 by weight) were dissolved in toluene with a total polymer concentration of 1- 5 wt%. To generate fluorescence contrast between PS and PMMA domains, 5-20 wt% of fluorescently-tagged PMMA was used, yielding a total of 2-8 wt% of PMMA chains end-labeled with Alexa Fluor 647 dyes. Solutions were stirred for 12 hr at room temperature prior to deposition of blend films via spin-coating with speeds of 1 or 3 krpm. Film thicknesses were controlled by varying the solution concentration and spin coating speed, and measured using ellipsometry (LSE Stokes Ellipsometer, Gaertner Scientific). Blend samples were prepared on silicon wafers or photo-etched square gridded cover slips (18x18 mm; Electron Microscopy Sciences) that were first cleaned with Piranha solution (7:3 concentrated sulfuric acid to 30% hydrogen peroxide solution) and then were exposed to oxygen plasma for 30 min. Gridded cover slips allowed us to locate the same region in fluorescence and AFM imaging.

### 2.3 Characterization of polymer blends by SEM and AFM:

For SEM imaging, the PMMA-rich phases were etched from blend films by immersing spin-coated films in acetic acid for 2 min. Samples were coated by a thin layer of gold, then imaged using an FEI Magellan 400 FESEM operated at 5 kV accelerating voltage and 30 pA

beam current. The surface structures of PS/PMMA blend films were examined using AFM (Digital Instruments, Dimension 3100) operated in tapping mode.

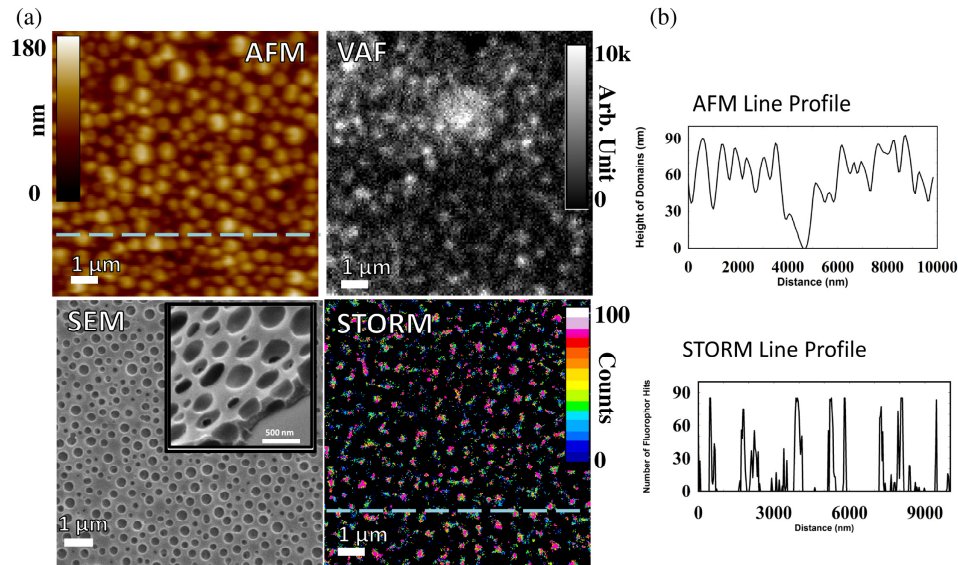


Fig. 1. Characterization of PS/PMMA blend films using four different techniques. (a) Atomic Force Microscopy (AFM), Scanning Electron Microscopy (SEM), Variable Angle Fluorescence (VAF), and Stochastic Optical Reconstruction Microscopy (STORM). Images were taken of 280 nm thick samples, except for SEM that was taken of 260 nm thick sample, and are displayed at the same magnification. In the AFM height image, the PMMA-rich domains (bright) are surrounded by the PS-rich phase (dark). In SEM, the PMMA-rich domains were extracted by selective solvent, and the remaining PS matrix is visualized. Inset shows a high magnification SEM image. In VAF and STORM, the bright spots result from fluorophores in the PMMA-rich domains. VAF and STORM images were taken on the same sample in the same region (Media 1). (b) Line scans through AFM and STORM images are taken from dashed lines across the images. The line profiles show the distribution of domains through the samples.

#### 2.4 STORM imaging methods

The STORM imaging system is a home built multi-laser system built around a Nikon Ti-E inverted microscope with 405, 488, 514, 561, and 647 nm wavelength lasers (maximum laser intensity 100 mW, except 488 maximum intensity of 60 mW) co-aligned through an Acousto-Optical Tunable Frequency (AOTF) crystal. In this study we used the Alexa Fluor 647 STORM dye [6], excited and imaged with a power density of  $\sim 5$  mW/mm<sup>2</sup> at the sample. The emission fluorescence was obtained using an Andor iXon Duo-648 EMCCD. We used a 60x oil objective, numerical-aperture 1.49 (Nikon), combined with objective magnifying lenses to obtain a 71 nm/pixel ratio. Because the refractive index of the polymer blend ( $\sim 1.5$ ) is close to the refractive index of glass, we used Variable Angle Fluorescence (VAF), rather than Total Internal Reflection Fluorescence (TIRF), to maximize signal to background, (Fig. 1). Exposure times were typically 30 – 100 ms, and imaging was continuous without shuttering. For data analysis, we used the quickPALM plugin [23] for ImageJ software [24]. A typical sample set consisted of 10,000 frames and was captured in 5-17 min. A single reconstruction image took 2-4 h of computation time to recreate. The typical fluorophore had a full-width-half-maximum (FWHM) of 3 pixels and signal-to-noise (SNR) of 1.0, where SNR is effectively defined as signal divided by the image noise-standard-deviation [23].

Because STORM is a stochastic readout method [21], thresholding methods were employed. First, fluorophore intensity per blink ( $m$ ) is stochastic; some fluorophores are brighter than others, due to local variations in excitation beam intensity, position relative to

the focal plane, orientation of fluorophore, nature of the local environment, or overlap with other PSFs. To account for variations, a brightness threshold is chosen using the SNR option in quickPALM. Consequently, thresholding results in an inherent non-linearity in the reconstruction: domains closer to the focal plane or tagged with more fluorophores will have more hits. Therefore, some domains will be better defined than others, as described previously [21]

Individual fluorophore counts within PMMA domains were non-uniform, so we set a minimum lateral size threshold to designate a domain. A typical localization resolution for individual fluorophores was  $\sim 40$  nm for our system. Therefore, a minimum domain size of 40 nm was chosen for our analysis. Domains smaller than 40 nm were excluded from domain size distribution calculations. Further, a minimum of 40 continuous counts within the boundaries was required. However, the requirement for at least 40 fluorophores per domain did not exclude any domains observed.

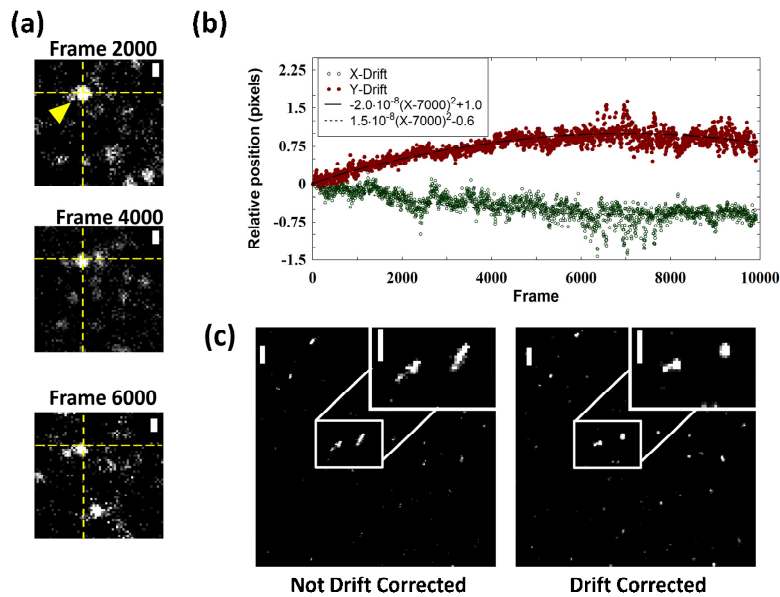


Fig. 2. The drift correction procedure using an aggregate fiduciary marker. (a) A single fiduciary marker drifts an appreciable amount over the experiment. The crossed, dashed lines, and yellow arrow indicate the location of the particle at frame 2000 with respect to images taken at frames 2000, 4000, and 6000. (Each frame was 100 ms). (b) The x-y drift is characterized and fit using a non-linear function, quadratic for this sample. Individual image frames were translated according to the fit equation. (c) Two domains within a single region are compared with and without drift correction. All images were taken from a 50 nm thick sample. Scale bars indicate 400 nm.

### 2.5 Sample Drift Correction

Sample drift is a significant problem in super-resolution imaging and is exacerbated by temperature shifts [27]. Drift can easily be corrected with fiduciary markers on the surface, either artificial or inherent. Since our samples were spin-coated, we did not want to introduce perturbing fiduciary markers that could shed fluorophores in the sample. Instead, we used regions of many brightly fluorescent fluorophores that were found to occur naturally in the sample. These regions occur randomly, perhaps due to aggregation of small amounts of

fluorophores not tagged to polymer chains. By imaging and tracking these locations, we were able to correct for drift.

Using such fluorophore aggregates for drift correction requires particular considerations because the fluorophores continued to blink and bleach during imaging. Such activity caused shifting center of mass, non-linear translation, and inaccuracy of localization of the aggregate over time (Fig. 2a). Fluorophore blinking resulted in a fluctuation of the apparent aggregate position that is un-related to true sample motion. Further, photo-bleaching of fluorophores within the aggregates resulted in un-predictable shifts in the center of mass. To correct for both of these effects, we used an average based on the positions of several fiduciary markers that would cancel random fluctuations of individual fiduciary aggregates.

Figure 2 shows an example fiduciary marker and surrounding domains of blinking fluorophore, over several frames. After the average fiduciary marker shift was determined, raw data were drift corrected *before* reconstruction analysis. We found that the drift of the sample was non-linear in time. We shifted individual frames based on a polynomial fit of the non-linear drift in x and y (Fig. 2b). Consequently, the raw data was corrected by translating each frame of the image sequence by the fit function of the fiduciary marker. Note that sub pixel translations are performed using the interpolation routine in ImageJ. Finally, the translation corrected image sequence is used for reconstruction analysis. Without drift correction, the sample shows a clear directional distortion of the domains, whereas the drift corrected data show less distortion (Fig. 2c).

### 3. Results and discussion

#### 3.1 Comparison of imaging methods

PS/PMMA samples were characterized by the standard techniques of AFM, SEM, and epi-fluorescence using VAF, to provide a comparison with results from STORM imaging. Figure 1 shows data obtained using the four techniques to characterize samples with very similar thicknesses (260 - 280 nm). AFM analysis provides excellent surface domain structure information, but does not reveal any information on structures below the surface. SEM of a similar sample shows consistent information on the sizes of and spacing between domains. An SEM image near a fractured sample edge (Fig. 1a, SEM inset) provides some degree of three-dimensional information on the cavities left after etching out the PMMA domains. The sample is essentially destroyed by the required etching, coating, and imaging procedures, thus precluding characterization by other techniques or *in situ* imaging of changes to the material. Wide field epi-fluorescence, or variable angle fluorescence (VAF), a standard optical microscopy fluorescence imaging technique has limited spatial resolution (Fig. 1a). In PS/PMMA samples VAF clearly shows some phase separation, as seen in the bright fluorescence spots. However, VAF cannot distinguish domains less than are smaller than the diffraction limit or in close proximity, resulting in overlapping intensities. STORM reconstruction and corresponding line-profile provides similar resolution as AFM without requiring invasive sample modifications (Fig. 1b).

#### 3.2 Imaging buffer effects

We developed a glycerol based imaging solution, because we observed a complete loss of fluorescence intensity when samples were exposed to the aqueous STORM buffer used in biological systems [11]. We suspect the loss of intensity was due to rapid bleaching of the fluorophores and/or a large reduction in their fluorescence intensities. After addition of the glycerol solution, blinking of some fluorophores was observed, and reconstruction images were able to be obtained. The glycerol based buffer contained the same essential ingredients as the aqueous buffer, including the oxygen scavenging system (OSS), glucose oxidase and catalase solution to limit oxidation and photo-bleaching, and  $\beta$ -mercaptoethanol ( $\beta$ ME) as a reducing agent that instigates fluorophore blinking helping the fluorophore move to the non-

fluorescent “dark” state. Because glycerol based solutions have not previously been used, we analyzed the effects by varying the concentration of individual components. In the original formulation of the imaging buffer used for biological samples, both the OSS and  $\beta$ ME are in concentrations of 0.7% (V/V) [11, 21]. In our imaging solution, both components are dissolved in 90% glycerol with 0.05M NaOH, at pH neutral as measured with pH paper.

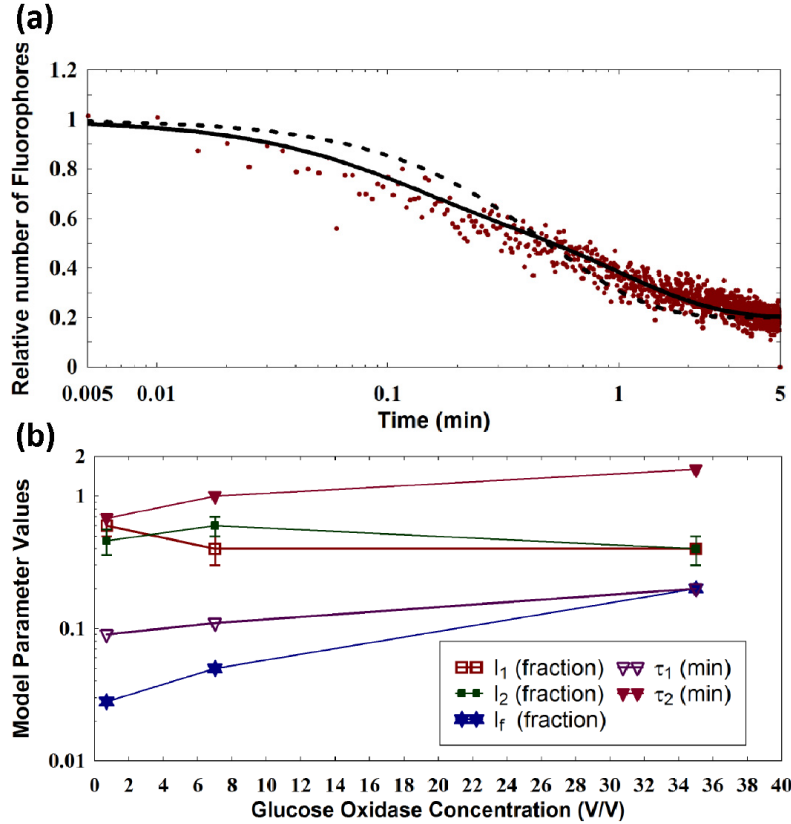


Fig. 3. Characterization of glycerol-based imaging buffer. (a) The fluorophore lifetime was determined by fitting the normalized fluorescence intensity, proportional to the number of fluorophores, over time to a double exponential decay function (solid line,  $R^2 = 0.8874$ ). A single exponential function (dotted line) did not accurately fit the data as well ( $R^2 = 0.7946$ ). (b) The parameters of the exponential functional fit are plotted as a function of OSS concentration. The fluorophore lifetimes,  $\tau_1$  and  $\tau_2$ , clearly increase with increasing OSS concentration, indicating that OSS is a limiting component.

We quantified the effects of our glycerol-based imaging buffer on fluorophore lifetime by measuring the relative number of fluorophores in a  $30 \times 30 \mu\text{m}$ -square region as a function of time (Fig. 3a). We then fit the loss of intensity ( $I$ ) to a double exponential decay:

$$I = I_1 e^{-\frac{t}{\tau_1}} + I_2 e^{-\frac{t}{\tau_2}} + I_f \quad (1)$$

where  $I_1$ ,  $I_2$  are the relative intensities of processes with decay times  $\tau_1$ ,  $\tau_2$ , respectively, and  $I_f$  is the final steady-state intensity. The origin of this multi-exponential decay is not clear, though we note that it may reflect differences in the accessibility of different domains to the imaging solution, as well as the competing rates of consumption and mass-transport of the

anti-oxidants. Over the time scale of our experiments, the intensity reaches a steady state value  $I_f$ , however, this population of fluorophores will also presumably photobleach over sufficiently long acquisition times.

We tested the fluorophore lifetime under various concentrations of OSS and  $\beta$ ME (Fig. 3b). First, the concentration of  $\beta$ ME was increased from 0.7 to 35% (V/V) while the concentration of OSS was held constant at 0.7%. The fluorophore lifetime did not change with increasing  $\beta$ ME, possible because  $\beta$ ME instigates the fluorophore dark state, and has a smaller effect on the ability of the fluorophore to photobleach. As expected,  $\beta$ ME had little effect on fluorophore lifetime. When the concentration of OSS was increased from 0.7 to 35% (V/V), while the concentration of  $\beta$ ME was held fixed at 0.7%, fluorophore lifetime significantly improved (Fig. 3b). Of the concentrations we tried, we found the 35% OSS had the longest lifetimes and significantly increased the number of long-lived fluorophores ( $I_f$ ), indicating that the background OSS concentration is sufficient to increase the number of fluorophores in the steady state. Further, the mean lifetimes for each state ( $\tau_1$ ,  $\tau_2$ ) increase by a factor of two. Since OSS is known to inhibit photobleaching, it is expected that the lifetimes will increase with increasing OSS concentration, as we observed. Both fluorophore life-time and survival fraction are important quantities to know because STORM resolution is dependent on the number of fluorophores in the sample. If the fluorophores are photobleaching too quickly, then a good reconstruction will take longer to obtain or could be unachievable.

Although we have found an imaging solution that was workable for our measurements, it is by no means optimized. Future explorations could explore the effects due to systematic alterations in both  $\beta$ ME and OSS concentrations. Further, we expect that the protein-based OSS developed for biological samples may not be the best anti-oxidant system for materials systems. We hope that future studies will explore other small molecule anti-oxidants and reducing agents that may be better compatible with the polymeric materials being studied.

### 3.3 Domain size determination

After reconstructing the STORM images, we characterized phase separated PMMA domains. For the most consistent comparison, the same PS/PMMA samples were imaged with AFM as well as STORM using the same gridded coverslips in the same regions within 30  $\mu$ m. Because the AFM imaging and the fluorescence imaging were performed on two different instruments, the gridded cover glasses enabled us to be in the same general region, although we were not able to directly correlate the AFM and fluorescence images. Future studies using an instrument with both AFM and fluorescence imaging could allow correlation between the two measurements to 70 nm.

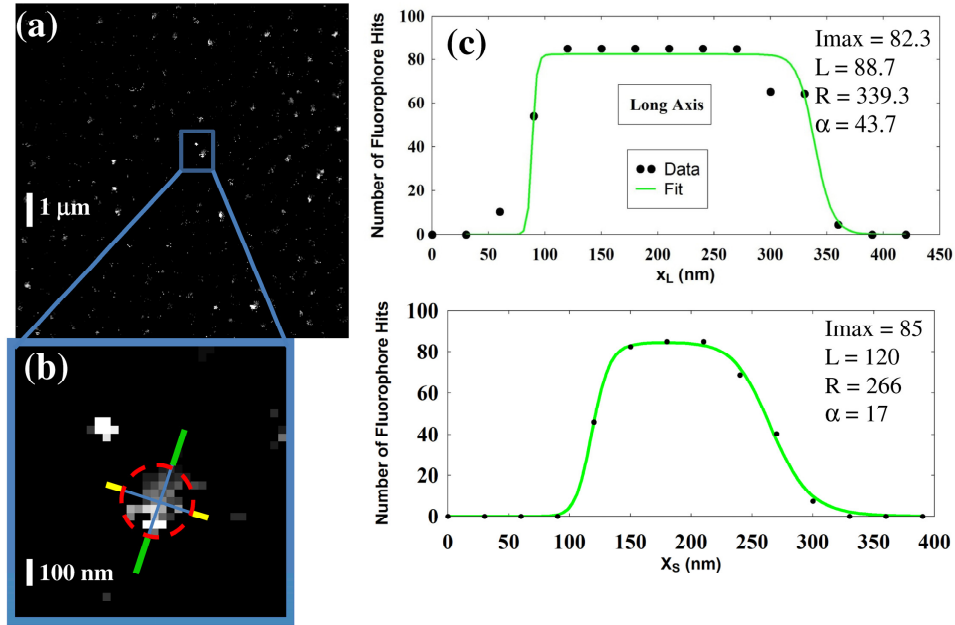


Fig. 4. Method for fitting PMMA domains in the reconstructed STORM images. (a) Low magnification image of multiple domains in a 280 nm sample. (b) A single domain at higher magnification shows the identified “long axis” (green line) and corresponding perpendicular “short axis” (yellow line). The dashed, red circle represents a circular domain with diameter equal to the long-axis. (c) Line profiles along the long axis and short axes were fit using Eq. (2). The fits of a single domain show one of the most extreme cases on the 280 nm sample thickness.

In order to determine the size of the domains, we performed a line scan through the longest cross-section of the image of the domain to measure the intensity as a function of distance (Fig. 4b). The intensity profiles were fit using the form:

$$I = I_{max} \left[ \frac{1}{1 + \left(\frac{x}{L}\right)^\alpha} - \frac{1}{1 + \left(\frac{x}{R}\right)^\alpha} \right] \quad (2)$$

where,  $I_{max}$  is proportional the number of fluorophore hits in the domain,  $L$  and  $R$  are the locations of the left and right walls of the domain, and  $\alpha$  is the slope of the wall (Fig. 4c). This function provides a good estimation of the lateral domain length with goodness of fit close to 1 ( $R^2$  ranged 0.90 – 0.99).

### 3.4 Domain size vs. sample thickness:

The domain size measured from the intensity profile of the long axis of the domain increased as a function of sample thickness (Fig. 5). This was expected because more extensive domain coarsening is possible in thicker samples due to the slower evaporation of solvent during film casting [28–31]. In addition to measuring the width of the long-axis, we also measured the width of the intensity profile of the perpendicular axis, which we call the “short axis,” using the same method (Eq. (2), Fig. 4). We find that, in STORM imaging, the domain shape becomes more asymmetric with increasing sample thickness (Fig. 5a). For instance, the 50 nm thick sample shows small and circular domains throughout the region, whereas the domains become more irregular for the 150 nm and 280 nm samples. Such irregularity was

not observed in SEM or AFM. We speculate that the difference may be due to the fact that in AFM and SEM the top surface that formed exposed to air interface is imaged, while in STORM the bottom surface close on the cover glass is imaged, and the domain shape may be affected by the presence of the glass.

Quantitatively, we found significant variability (~50-70%) in the short-axis results, across different domains. Some were very circular, while others were very thin. Further, where the short-axis cross-section is chosen results in a large uncertainty. Therefore, we chose not to include the short-axis in our analysis, rather we chose to compare the long-axis when comparing to AFM domain distributions (Fig. 5).

Quantitative domain size results obtained by STORM are consistent to domain size results obtained by AFM (Fig. 6a). Samples were first imaged using AFM (Fig. 6a, open symbols) followed by analysis using STORM (Fig. 6a, solid symbols) in the same general region within the same 30  $\mu\text{m}$  enabled by the use of gridded coverslips. From both techniques, it is clear that the lateral domain size and the width of the size distribution linearly increase with sample thickness, in the range of 50 – 360 nm (Fig. 4b, 6a). More importantly, the increases in average domain size and width distribution are consistent in both techniques (Fig. 6a). Thus, this model PS/PMMA system proves that STORM can provide quantitative structural information similar to AFM. Furthermore, STORM could be extended to provide structural information below the surface, unlike AFM.

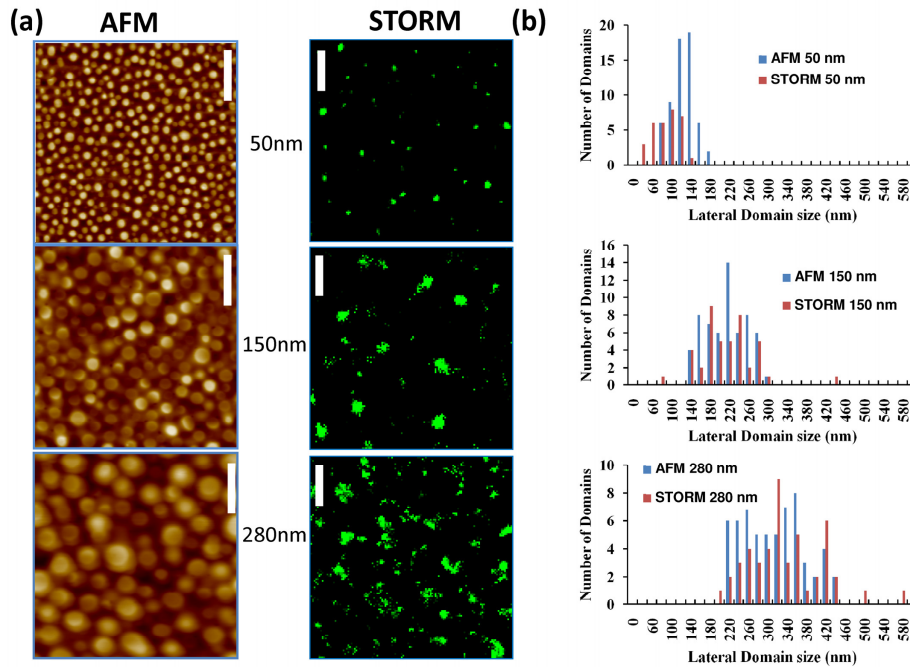


Fig. 5. Domain size distribution. (a) Sample regions of AFM and STORM images for different sample thicknesses: (i) 50 nm, (ii) 150 nm, and (iii) 280 nm thick samples. All scale bars are 400 nm. (b) The distribution of domain sizes for STORM and AFM analysis, as a function of sample thickness. The STORM data show increasing domain size distribution consistent with AFM.

Despite excellent domain size agreement, the density of domains was markedly different between the techniques (Fig. 6b). Domain density was determined by counting the number of domains within a 5 x 5  $\mu\text{m}$  region. AFM analysis shows a decreasing domain density with increasing sample thickness (Fig. 6b, solid circles), as expected. Further, this is consistent with SEM analysis for larger sample thicknesses (Fig. 6b, solid stars). However, STORM

analysis shows significantly lower domain density (Fig. 6b, solid triangles); the scale difference is a factor of 4.5 (Fig. 6b, diamonds). Despite the difference, the STORM data shows the same dependence of the density as a function of sample thickness, which suggests that the scale factor difference is related to the STORM technique itself.

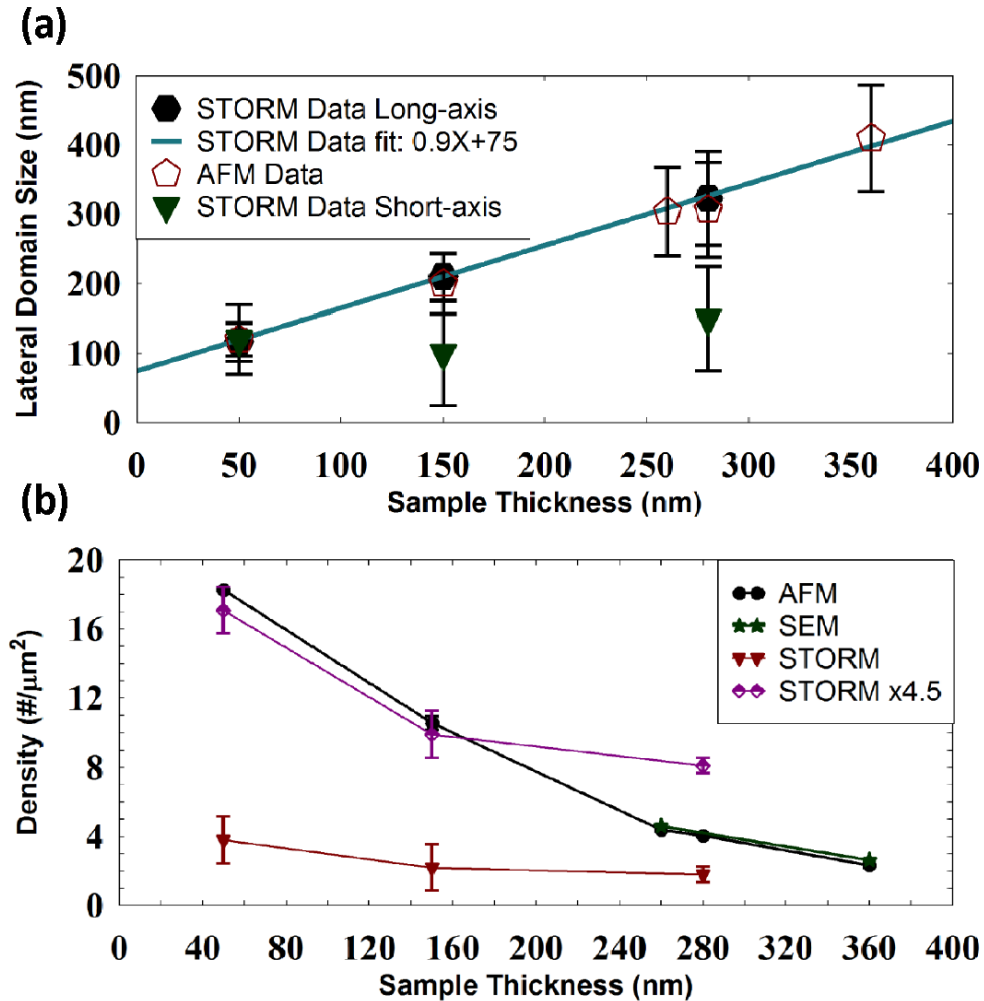


Fig. 6. Lateral domain size and domain density comparison to AFM results. (a) Comparing the long-axis lengths obtained by STORM to AFM shows equivalent behavior and quantitative agreement. The best fit is a line with slope of  $0.9 \pm 0.2$  and intercept of  $75 \pm 15$  nm ( $R^2 = 0.9996$ ). (b) The domain densities, as a function of sample thickness, are compared for different techniques, and it is apparent that STORM undercounts the number of domains compared to SEM or AFM, which agree.

We speculate that the domain density difference between STORM and AFM analysis is related to the cumulative effects of sample imaging geometry and fluorophore life-time. One possible reason for the missing domains is that we imaged with an inherently non-uniform illumination intensity profile over the x-y imaging plane in due to the laser. Non-uniform illumination results in inconsistent stochastic blinking, because fluorescence on/off statistics are strongly dependent on illumination intensity [3]. We chose to not make the incident illumination uniform across the field because doing so would cause a loss of intensity, resulted in even fewer blinking fluorophores.

Another possible explanation is the geometric differences between AFM, SEM, and STORM imaging. AFM and SEM image the top surface where the blend film interacts with the air. STORM and VAF imaging occur at the cover glass surface. There may be irregularly shaped or fewer domains at the cover glass than at the air interface. Such differences are only hinted at in the SEM cross-section and the VAF image (Fig. 1a). In VAF, many of the possible PMMA domains are dim implying that they may be away from the illumination region of the laser. As described above, low illumination intensity will lead to reduced blinking of the fluorophores in those domains. The quickPALM software only fits blinking fluorophores and discards fluorophores that are always on or always off, so dim domains are not likely to be included in the STORM reconstruction. An examination of the raw image data from the data presented in Fig. 1 shows that, although blinking is observed, many domains are permanently fluorescent and are not being included in the reconstruction (Media 1); for example, the circled domain shows a fluorophore aggregate which does not exhibit blinking, whereas the square outlined domain showing blinking fluorophores.

Together, these effects combine such that regions of the image plane with less illumination intensity may not be well characterized in the reconstructed image. In future studies, we may be able to observe more of these domains if we have higher laser power to cause the fluorophores in these domains set back from the surface to go into the dark state. Another option is to forgo VAF illumination and instead use the collimated laser directly through the sample to deplete the entire sample thoroughly. We found VAF helped reduce background when fitting single particles, but other angles or illumination schemes may prove worthwhile.

#### 4. Conclusion

We have demonstrated that STORM imaging gives nearly equivalent quantitative results on the sizes of demixed domains for a model PS/PMMA polymer blend film compared to AFM imaging. Our results suggest that STORM imaging could be a valuable tool for dissecting the nanoscale structure of synthetic material systems in the future. STORM has the further advantage of being a non-invasive and non-destructive, and unlike AFM, STORM could capture dynamics. However, STORM is limited in the time scales accessible: between 30 seconds to 15 minutes depending on the exposure time and number of frames needed to accurately reconstruct an image. Future studies should focus on optimization of fluorophore loading and imaging conditions for synthetic material systems, make use of the three-dimensional reconstruction capabilities of STORM, and explore opportunities for in situ measurements of structural evolution.